

# Inhibition of a Protein Tyrosine Phosphatase Using Mesoporous Oxides<sup>†</sup>

S. Kapoor,<sup>‡</sup> T. S. Girish,<sup>§</sup> S. S. Mandal,<sup>‡</sup> B. Gopal,<sup>§</sup> and A. J. Bhattacharyya<sup>\*,‡</sup>

Solid State and Structural Chemistry Unit, and Molecular Biophysics Unit, Indian Institute of Science, Bangalore 560012, India

Received: October 24, 2009; Revised Manuscript Received: February 07, 2010

The feasibility of utilizing mesoporous matrices of alumina and silica for the inhibition of enzymatic activity is presented here. These studies were performed on a protein tyrosine phosphatase by the name chick retinal tyrosine phosphatase-2 (CRYP-2), a protein that is identical in sequence to the human glomerular epithelial protein-1 and involved in hepatic carcinoma. The inhibition of CRYP-2 is of tremendous therapeutic importance. Inhibition of catalytic activity was examined using the sustained delivery of *p*-nitrocatechol sulfate (pNCS) from bare and amine functionalized mesoporous silica (MCM-48) and mesoporous alumina (Al<sub>2</sub>O<sub>3</sub>). Among the various mesoporous matrices employed, amine functionalized MCM-48 exhibited the best release of pNCS and also inhibition of CRYP-2. The maximum speed of reaction  $v_{\max}$  ( $=160 \pm 10 \mu\text{mol}/\text{mnt}/\text{mg}$ ) and inhibition constant  $K_i$  ( $=85.0 \pm 5.0 \mu\text{mol}$ ) estimated using a competitive inhibition model were found to be very similar to inhibition activities of protein tyrosine phosphatases using other methods.

## 1. Introduction

Receptor-protein mediated interactions play essential roles in most developmental processes.<sup>1–7</sup> The mechanisms by which these proteins are regulated have been under intense investigation to understand the molecular basis for their activities, as well as for important biomedical applications. Receptor-protein activation is brought about by selective phosphorylation of cytoplasmic components of the receptor, usually several tyrosine residues. The resulting signaling cascade is regulated by the presence of several protein tyrosine phosphatases (PTPs) that can modulate the signaling through dephosphorylation of the receptor. Thus, the ability to selectively control protein phosphatase activities is an important step in being able to regulate targeted signaling pathways. The ability to modulate phosphatase signaling activities in a sustained manner thus has immense biological and biomedical importance.

A major challenge to modulating the activity of a particular phosphatase in a cellular environment is the inherent specificity dominated by a phosphotyrosine moiety. There are four distinct classes of protein tyrosine phosphatases referred to as classical PTPs, dual-specificity PTPs, low molecular weight PTPs, and receptor protein tyrosine phosphatases (RPTPs). All these phosphatases have a unifying characteristic of binding a phosphorylated tyrosine in their active sites. There is very little information about the nature or role of the sites that confer secondary specificity. Recent studies have revealed that despite the extensive sequence and structure conservation, subtle variations in regions away from the active site can affect the activity of the phosphatase. Kinetic and crystallographic studies, for example, have suggested the tantalizing feature that it is possible to convert a PTP-1B to a PTP- $\alpha$  and vice versa by simply replacing the bulky Gln 259 in PTP-1B to a Gly. PTP-1B<sup>8</sup> inactivates insulin signaling by removing docking sites on the insulin receptor (IR) and disrupts STAT-5B dimers, whereas

PTP- $\alpha$  activates Src kinase by dephosphorylation of its auto-inhibitory phosphotyrosine involved in the intramolecular recognition by the Src SH2 domain. The dramatic effects of a single amino acid change is even more interesting because the presence of a Gly at position 259 in PTP-1B allows for the high affinity binding of substrates, such as the activation loop of the insulin receptor which contains two adjacent phosphotyrosine residues. This suggests the presence of a secondary substrate-binding pocket which engages the adjacent phosphotyrosine residue while the phosphotyrosine residue which does get phosphorylated attaches itself to the active site.<sup>9</sup> These studies suggest the possibility that novel allosteric inhibitors could be designed for this class of enzymes. This approach, however, requires a priori information on suitable allosteric sites on the catalytic domain that are specific to a given PTP domain. In this study, we demonstrate an alternative approach utilizing mesoporous matrices to deliver enzyme inhibitors. Unlike other modes of administration, chemical modification of the inhibitor is not a necessity with delivery systems. This is a major advantage as undue chemical modification of the inhibitor may lead to changes in the native structure and hence potency. Inorganic nanostructured oxide materials have already been demonstrated as potential controlled drug delivery systems (DDSs).<sup>10–17</sup> The key advantages of inorganic nanostructured materials are that their structures are able to resist degradation and hence facilitate release of pertinent molecules at requisite times and in requisite amounts unlike other forms, especially organic based delivery systems such as liposomes or polymers, which degrade prematurely leading to poor yields at the target site. Mesoporous material such as MCM41 was demonstrated as a DDS for the first time in 2001 by the group of Vallet-Regi et al.<sup>10</sup> Since then various mesoporous materials (MCM-41/-48, MSU, HMS) have been synthesized for the purpose of sustained drug delivery and also for several other biotechnological applications.<sup>11–13</sup> Mesoporous materials offer several attractive features such as (a) stable porous structure, (b) large surface area, (c) tunable pore sizes and volumes, and (d) easier chemical functionalization of the surface. All these features aid in better manipulation of guest uptake and release. In this work

<sup>†</sup> S.K. and T.S.G. contributed equally to this work.

<sup>\*</sup> Corresponding author. E-mail: aninda\_jb@sscu.iisc.ernet.in. Fax: +918023601310.

<sup>‡</sup> Solid State and Structural Chemistry Unit.

<sup>§</sup> Molecular Biophysics Unit.

we have employed bare and functionalized commercial mesoporous alumina and in-house synthesized MCM-48 silica to deliver *p*-nitrocatechol sulfate (pNCS), a potent competitive PTP inhibitor. pNCS was chosen as model inhibitor because of the ease of monitoring its release using UV–visible absorption spectroscopy. Oxide materials releasing pNCS at different rates lead to differential enzyme inhibition which was estimated using the activity assays. This study on the catalytic domain of CRYP-2 (also referred to as GLEPP-1/PTPRO<sup>18</sup>) serves to demonstrate the feasibility of inhibition of this enzyme. This study suggests the possibility of potential therapeutic applications in the case of this enzyme that is involved in cystogenesis and tumorigenesis in end-stage renal disease (ESRD) as well as demonstrates the potential of this strategy as a generic tool for sustained enzyme inhibition in specific cellular contexts.

## 2. Experimental: Materials and Methods

**Synthesis of MCM-48.** Cetyltrimethylammonium bromide (CTAB) (6.5 g) was mixed with 0.6 g of sodium hydroxide (NaOH) followed by addition of ethanol. Tetraethyl orthosilicate (TEOS) was added dropwise to the solution while stirring (rotation speed  $\sim 400$  rpm). Following addition of TEOS the solution was stirred for 1 h. The white sol so obtained was put in an autoclave which was heated at 140 °C for 23 h. After cooling, the contents were filtered off and subsequently washed with water. The white powder so obtained was dried first at 110 °C for 6 h followed by calcination at 550 °C for another 6 h in air. Specific surface area (BET) and pore-size distribution were obtained from nitrogen adsorption–desorption isotherms (Belsorp). The BET surface area for MCM-48 was found to be 998 m<sup>2</sup> g<sup>−1</sup>, and the average pore size was 2.5 nm (Supporting Information).

**Synthesis of Al<sub>2</sub>O<sub>3</sub>–NH<sub>2</sub> and MCM-48–NH<sub>2</sub> Oxide Materials.** Calculated amounts of commercially available Al<sub>2</sub>O<sub>3</sub> (Aldrich) and in-house synthesized MCM-48 (200 mg) were added to 10 mL of toluene and stirred continuously. One milliliter of the functionalizing moiety APTMS, i.e., 3-aminotrimethoxysilane, was added dropwise slowly into the stirred solution. The solution was aged for 24 h and then washed with an extra amount of toluene. After drying, the functionalization of the alumina surface with amine moiety was confirmed via Fourier transform infrared spectroscopy (FTIR). Room temperature ( $\approx 25$  °C) FTIR (Perkin-Elmer FT-IR Spectrometer Spectrum 1000) measurements were done with a requisite amount of sample mixed with pure spectroscopic grade potassium bromide (KBr) and cast into pellets of diameter 1.3 cm and thickness  $\sim 0.1$  cm. Amine functionalization of Al<sub>2</sub>O<sub>3</sub> surface was also studied using nitrogen adsorption–desorption isotherms. While the surface area decreased from 190 m<sup>2</sup> g<sup>−1</sup> for pure Al<sub>2</sub>O<sub>3</sub> to 95 m<sup>2</sup> g<sup>−1</sup> for Al<sub>2</sub>O<sub>3</sub>–NH<sub>2</sub>, it decreased from 998 m<sup>2</sup> g<sup>−1</sup> for MCM-48 to negligible values following amine functionalization.

**Production of Recombinant CRYP-2/PTPRO (Receptor-Type Tyrosine-Protein Phosphatase O).** Details of the cloning, expression, purification, and crystal structure determination of the catalytic domain of CRYP-2 protein have been described earlier.<sup>18,19</sup> Briefly, the cytosolic, catalytic domain of CRYP-2 (residues 956–1267) was cloned between the NheI and XhoI sites of the vector pET 22b (incorporating a polyhistidine tag at the C-terminus). After transforming the plasmids containing the appropriate insert into BL21(DE3) cells (Novagen, Inc.), the cells were allowed to grow to an optical density at 600 nm of 0.5 when the cells were induced with 0.5 mM IPTG (final concentration). Following this, the temperature for growth was

dropped down to 25 °C, and cells were further grown for 6 h before they were spun down. The cells were resuspended in lysis buffer (50 mM sodium phosphate buffer, 250 mM NaCl pH 7.5). After sonication for 4 min on ice, the cell debris was separated from the crude cell lysate by centrifugation (Sorvall Centrifuge) for 30 min at 10 000 rpm. After equilibration with the cobalt containing TALON (Clontech, Inc.) resin (approximately 4 mL of resin suspension for cell-free lysate from 10 g of cell paste) and a washing step with buffer B (50 mM sodium phosphate, 250 mM NaCl, 5 mM imidazole, pH 7.5), the N-terminal 6-His tagged CRYP-2 was eluted from the column using the elution buffer (50 mM sodium phosphate, 250 mM NaCl, 200 mM imidazole pH 7.5). The partially purified protein was further subjected to size exclusion chromatography on a Sephacryl Hiprep 16/60 S-200 HR column (Amersham Biosciences Inc.).

**Preparation of Oxide–pNCS Composites.** Ten milligrams of bare and functionalized Al<sub>2</sub>O<sub>3</sub>/MCM-48 particles was mixed with 10 mg of pNCS inhibitor in 1 mL of HEPES buffer (25 mM HEPES, 50 mM NaCl, 2.5 mM EDTA, and 5 mM DTT) and incubated at 4 °C for 24 h. After 24 h the solution was centrifuged, and the pellet was dried at 30 °C under vacuum.

**Release Kinetics of pNCS from Oxide–pNCS Composites.** Release of pNCS from Al<sub>2</sub>O<sub>3</sub>/Al<sub>2</sub>O<sub>3</sub>–NH<sub>2</sub>/MCM-48/MCM-48–NH<sub>2</sub>:pNCS was studied in HEPES buffer (pH 7) having the following composition: 25 mM HEPES, 50 mM NaCl, 2.5 mM EDTA, and 5 mM DTT. The concentration of all composites in HEPES buffer was approximately 1.33 mg mL<sup>−1</sup>. pNCS release kinetics was observed by monitoring the characteristic peak at 406 nm of pNCS by UV–vis spectroscopy. Aliquots were collected at regular intervals of time ( $\approx 1$  h) only for the matrices which showed a reasonably high amount of inhibitor release over a period of one day. The aliquots were immediately analyzed for the inhibition of phosphatase activity by following the protocol as described below.

**Kinetic Characterization of CRYP-2 Phosphatase Activity.** The phosphatase activity assays were performed using *p*-nitrophenyl phosphate (pNPP, C<sub>6</sub>H<sub>5</sub>NO<sub>6</sub>P,  $M_w = 219.09$ ) as substrate. The assay buffer consists of 25 mM HEPES, 50 mM NaCl, 5 mM DTT, and 2.5 mM EDTA at pH 7.0. The final reaction volume was 200  $\mu$ L, which was composed of 90  $\mu$ L bovine serum albumin (BSA –0.01% solution in assay buffer), 80  $\mu$ L of assay buffer, and a suitable amount of pNPP. The reaction was started by adding appropriately diluted CRYP-2 enzyme and was stopped after 10 min by addition of 100  $\mu$ L of 2.0 M Na<sub>2</sub>CO<sub>3</sub>. The total volume was made to 1000  $\mu$ L with distilled water. The activity was estimated by monitoring the absorbance at 405 nm of PNP product formed. The enzyme activity was calculated using the extinction coefficient of  $1.8 \times 10^4$  M<sup>−1</sup> cm<sup>−1</sup>. The kinetic parameters were determined by fitting initial velocity data to the Michaelis–Menten equation<sup>20</sup> by nonlinear regression analysis. For measuring the inhibition constant ( $K_i$ ) of *p*-nitrocatechol sulfate (pNCS, C<sub>6</sub>H<sub>5</sub>NO<sub>7</sub>S,  $M_w = 235.17$ ), CRYP-2 activity was measured at different concentrations of pNCS in the presence of varying concentrations of substrate (pNPP), and the data were analyzed by nonlinear regression analysis by fitting to a competitive inhibition model (Graphpad prism software).

## 3. Results and Discussion

**Characterization of the Oxide–Inhibitor Composites.**  
*i. Thermogravimetry Analysis.* Figure 2 shows the thermogravimetry analysis profiles for the oxide–inhibitor composites. The loading fractions of pNPS in all samples were estimated

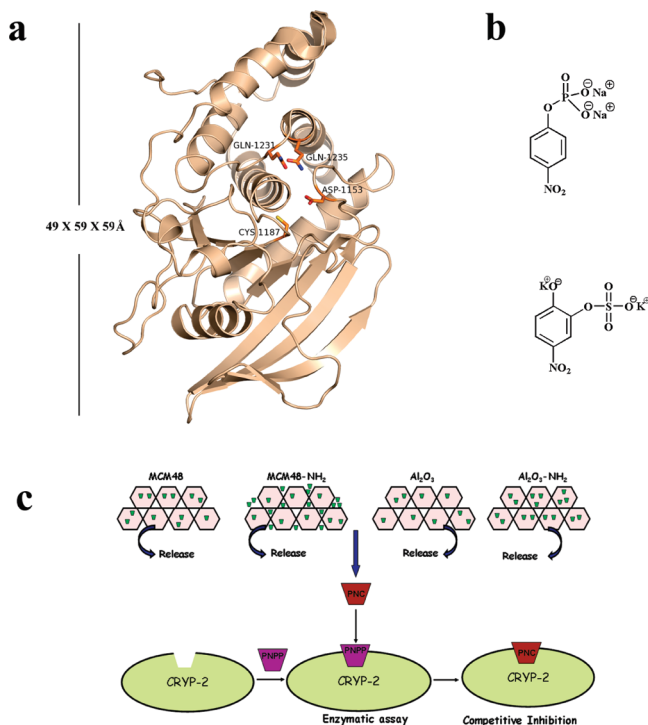


**Figure 1.** (a) Crystal structure of CRYP-2 with the dimensions mentioned on the left. The catalytically critical residues at the active site are shown as sticks. (b) Chemical structure of pNCS and pNPP. (c) Schematic representation of inhibitor (pNCS) release and inhibition of CRYP-2 catalyzed pNPP hydrolysis.

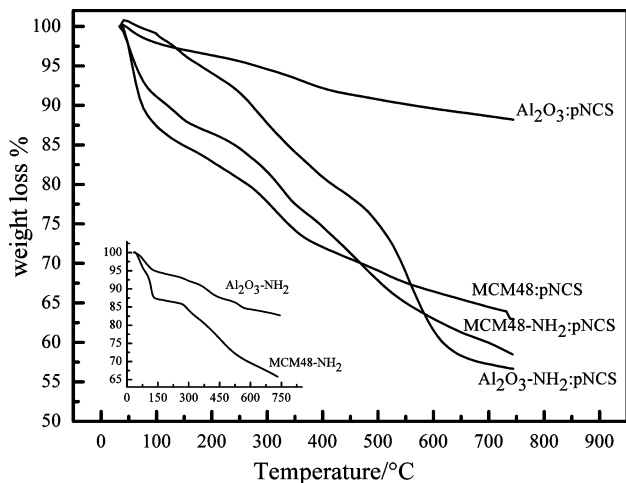


**Figure 2.** Thermogravimetry analysis (TGA) for Al<sub>2</sub>O<sub>3</sub>(OH):pNCS, Al<sub>2</sub>O<sub>3</sub>-NH<sub>2</sub>:pNCS, MCM-48:pNCS, and MCM-48-NH<sub>2</sub>:pNCS (temperature range, 25–750 °C; heating rate, 10 °C min<sup>-1</sup>).

from the ratio of weight loss between 190 and 750 °C. These were found to be 9% and 22% for pure Al<sub>2</sub>O<sub>3</sub> and MCM-48, respectively. For Al<sub>2</sub>O<sub>3</sub>-NH<sub>2</sub> and MCM-48-NH<sub>2</sub> the degree of loading was 41% and 31%, respectively. The weight loss due to organic group was 11% for Al<sub>2</sub>O<sub>3</sub>-NH<sub>2</sub> and 19% for MCM-48-NH<sub>2</sub>. This weight loss is attributed not only to the fraction chemically bound to the surface of mesoporous Al<sub>2</sub>O<sub>3</sub> and MCM-48 but also to those which are held physically. This shows that net loading of pNCS in Al<sub>2</sub>O<sub>3</sub>-NH<sub>2</sub> is approximately 30% and MCM-48 is found to be 12%.

**ii. Fourier Transform Infrared Spectroscopy.** Figures 3a and 3b show the FTIR spectra for Al<sub>2</sub>O<sub>3</sub> and MCM-48 inhibitor complexes. As shown in Figure 3a the band in the range of (3750–3000) cm<sup>-1</sup> is due to the Al–OH stretching frequency.<sup>21</sup>

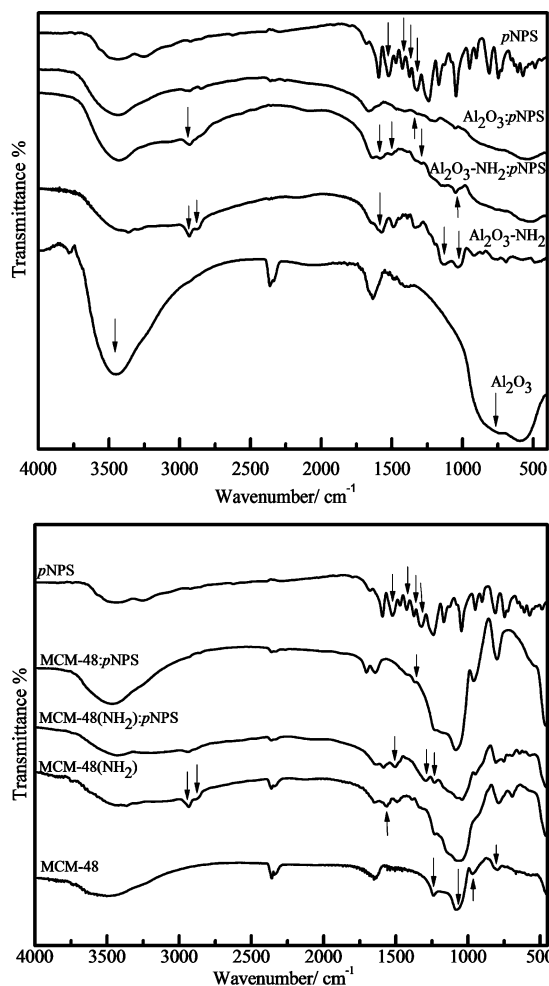


**Figure 3.** (a) Fourier transform infrared spectra at 25 °C for pNCS, Al<sub>2</sub>O<sub>3</sub>, Al<sub>2</sub>O<sub>3</sub>-NH<sub>2</sub>, Al<sub>2</sub>O<sub>3</sub>:pNCS, and Al<sub>2</sub>O<sub>3</sub>-NH<sub>2</sub>:pNCS. (b) Fourier transform infrared spectra at 25 °C for pNCS, MCM-48, MCM-48-NH<sub>2</sub>, MCM-48:pNCS, and MCM-48-NH<sub>2</sub>:pNCS.

The broad curvature band in the range (900–800) cm<sup>-1</sup> is due to Al–O stretching. The surface coverage by APTMS leads to new bands.<sup>22</sup> The bands at 1132 and 1028 cm<sup>-1</sup> are due to C–N stretch in aliphatic amines, whereas the bands at 2931 and 2876 cm<sup>-1</sup> are due to asymmetric and symmetric C–H stretch. Signature of N–H deformation is observed via the appearance of bands at 1574 cm<sup>-1</sup>. Appearance of these bands confers successful functionalization of alumina surface by APTMS. As shown in Figure 3a and 3b bands for pNCS appearing in the range of (1550–1475) and (1360–1290) cm<sup>-1</sup> are due to N–O asymmetric and symmetric stretching, respectively. The bands at 1377 and 1425 cm<sup>-1</sup> are due to SO<sub>3</sub> stretch. The bands in the range (1335–1250) cm<sup>-1</sup> are observed due to C–N stretching in pNCS. For Al<sub>2</sub>O<sub>3</sub>:pNCS the C–N stretching band is observed at 1330 cm<sup>-1</sup>, whereas for Al<sub>2</sub>O<sub>3</sub>-NH<sub>2</sub>:pNCS it is observed at 1293 cm<sup>-1</sup> and is less intense suggesting stronger interaction of Al<sub>2</sub>O<sub>3</sub>-NH<sub>2</sub> with pNCS and slower release of pNCS from Al<sub>2</sub>O<sub>3</sub>-NH<sub>2</sub>:pNCS compared to Al<sub>2</sub>O<sub>3</sub>-OH:pNCS. Figure 3b shows the FTIR for MCM-48 samples. For MCM-48, bands seen at 1236, 1084, and 804 cm<sup>-1</sup> are due to Si–O–Si vibrations while the band at 964 cm<sup>-1</sup> is due to Si–OH vibrations. For MCM-48-NH<sub>2</sub> new bands are observed at 2934 and 2878 cm<sup>-1</sup> due to asymmetric and symmetric C–H stretching. The 1564 cm<sup>-1</sup> band is due to N–H deformation. The appearance of these bands too confirms functionalization of silica surfaces with APTMS. The characteristic bands of



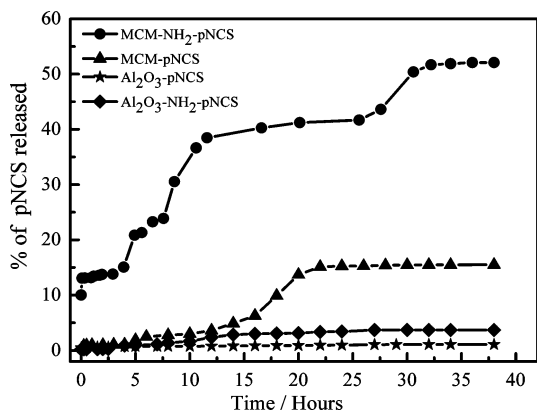


**Figure 4.** Release kinetics of pNCS (into HEPES buffer at 25 °C) from  $\text{Al}_2\text{O}_3/\text{Al}_2\text{O}_3\text{-NH}_2/\text{MCM-48}/\text{MCM-48-NH}_2$  and inhibition.

pNCS (N–O asymmetric and symmetric stretch) are present for MCM-48- $\text{NH}_2$ :pNCS sample but absent for MCM-48:pNCS suggesting that pNCS is completely inside the pores of MCM-48. Functionalization with APTMS results in reduction of pore size (functionalization of MCM41 with APTMS resulted in reduction of pore size from 2.5 to 1.7 nm<sup>23</sup>), which may lead to residence of a certain fraction of pNCS outside the MCM-48 pores. We suppose that pNCS molecules are held close to the surface via electrostatic interactions between the positively charged  $\text{NH}_2$  group and negatively charged pNCS. This causes detection of characteristic bands of pNCS in MCM-48 ( $\text{NH}_2$ ): pNCS sample.

**iii. In Vitro Release Kinetics.** Figure 4 shows the in vitro release kinetics of  $\text{Al}_2\text{O}_3$ :pNCS,  $\text{Al}_2\text{O}_3\text{-NH}_2$ :pNCS, MCM-48:pNCS, and MCM-48- $\text{NH}_2$ :pNCS. For  $\text{Al}_2\text{O}_3$ :pNCS the yield of pNCS in solution after 38 h was approximately 158  $\mu\text{M}$  (saturation time, approximately 13 h), whereas for MCM-48:pNCS it was 197  $\mu\text{M}$  (saturation time, approximately 20 h). The higher yield of pNCS in buffer solution in the case of MCM-48 compared to  $\text{Al}_2\text{O}_3$  can be attributed to the higher degree of pNCS loading inside MCM-48 than that of  $\text{Al}_2\text{O}_3$ . The release of guest molecule depends on the host pore size and structural arrangement and also on the strength of chemical interaction between host matrix and guest molecule. Irrespective of the structural configuration of the pores, it is in general difficult for the solvent to solvate the guest molecules out of smaller sized pores of the host matrix. In addition, smaller pore size results in higher probability for the guest molecules to reside outside the mesopores in the region between the oxide particles forming larger aggregates. The solvation argument also holds if strong interaction exists between the host and matrix. In the present work, since  $\text{NH}_2$  is more basic compared to OH, the interaction with pNCS will be stronger in the former leading to slower and lower yields. However, functionalization results in additional decrease in effective pore size leading to decrease in pNCS yields inside the matrix. pNCS loading in pure  $\text{Al}_2\text{O}_3$  is low (= 9%) compared to MCM-48 (22%). The poor release yield ( $\approx 1\%$ ) in pure  $\text{Al}_2\text{O}_3$  is mainly due to low degree of pNCS loading in  $\text{Al}_2\text{O}_3$  and also predominant residence of pNCS in pores of size  $\sim 2$  nm or smaller. For  $\text{Al}_2\text{O}_3\text{-NH}_2$ , pNCS loading (=30%) and release is slightly higher ( $\approx 2.5\%$ ) compared to pure  $\text{Al}_2\text{O}_3$ . This is probably due to release of pNCS residing outside the pores due to pore size reduction following functionalization. However, strong interaction between pNCS and oxide surface prevents any additional release. The release from MCM matrices are much higher compared to  $\text{Al}_2\text{O}_3$ . The approximate pore size equals 2.5 nm for MCM-48 and becomes very small in size with the majority of them getting completely

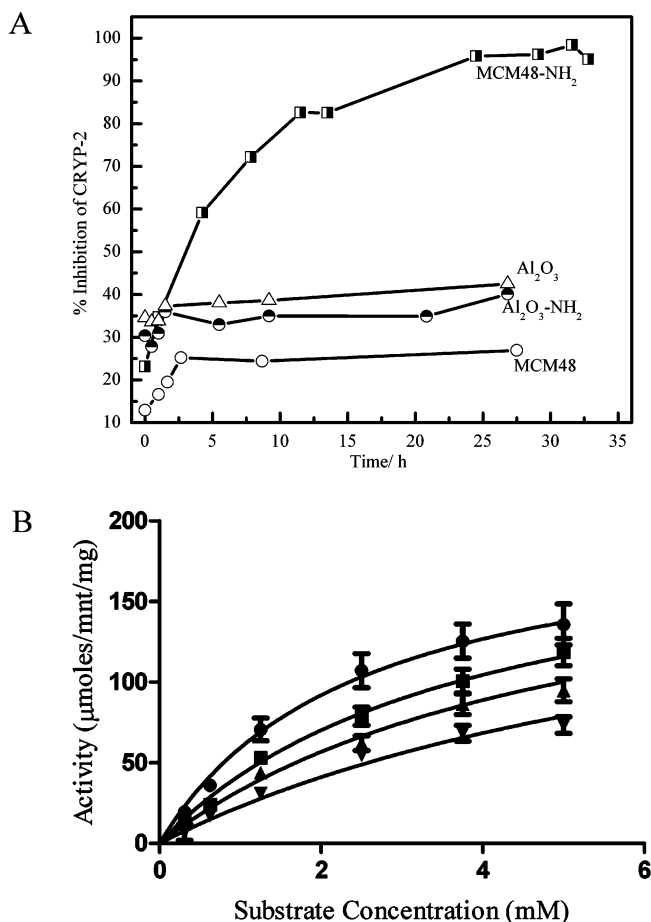


**Figure 5.** (A) Inhibition kinetics of pNCS from  $\text{Al}_2\text{O}_3/\text{Al}_2\text{O}_3\text{-NH}_2/\text{MCM-48}/\text{MCM-48-NH}_2$ . (B) Effect of pNCS on the CRYP-2 catalyzed pNPP hydrolysis. The Michealis–Menten plots carried out in the presence of varying concentrations of pNCS: 0  $\mu\text{mol}$  (●), 50  $\mu\text{mol}$  (■), 100  $\mu\text{mol}$  (▲), and 200  $\mu\text{mol}$  (▼) indicate competitive inhibition of CRYP-2 activity by pNCS with a inhibition constant of  $85 \pm 5$   $\mu\text{mol}$ .

blocked (Supporting Information) following amine functionalization. In the case of MCM matrices, a significant fraction of pNCS resides outside the pores in the region between the oxide particles forming larger aggregates. This results in higher ( $\approx 15\%$ ) and faster release compared to bare and functionalized  $\text{Al}_2\text{O}_3$ . In the case of MCM-48- $\text{NH}_2$ , it is envisaged that almost all of the pNCS lies outside, and hence this system displays the best pNCS release ( $\approx 50\%$ ). Thus, matrix is also expected to show the best enzyme inhibition.

**iv. Phosphatase Activity and pNCS Inhibition of Phosphatase Activity.** The purified enzyme was examined for catalytic activity with pNPP under conditions reported earlier.<sup>18</sup> The  $v_{\text{max}}$  and  $K_{\text{m}}$  values obtained by fitting rate versus substrate plots (not shown here) of the Michaelis–Menten equation<sup>20</sup> for CRYP-2 are  $160 \pm 10$   $\mu\text{mol}/\text{mnt}/\text{mg}$  and  $1.33 \pm 0.15$  mM, respectively. A comparison of the phosphatase activity of CRYP-2/PTPRO with two other PTPs is shown in Supporting Information Table 1. The similar parameters for catalytic activity seen in this comparison thus suggest that the inhibition kinetics reported in this study would be broadly applicable to other PTPs as well. The pNCS having similar chemical structure as that of pNPP (Figure 1b) has been reported to inhibit protein tyrosine phosphatase with inhibition constant  $K_{\text{i}} \sim$  a few tens of micromoles. In order to determine the effect of pNCS, released from a mesoporous matrix, on phosphatase activity of CRYP-2, pNPP hydrolysis assay was carried out in the presence of

varying concentrations of pNCS (50, 100, and 200  $\mu\text{M}$ , Figure 5). The inhibition of CRYP-2 by pNCS was carried out immediately after its collection (as aliquots) during in vitro release from MCM-48-NH<sub>2</sub> matrix. Inhibition study was done with MCM-48-NH<sub>2</sub> only as it exhibited the highest release of pNCS among all the matrices employed. The observed variation in activity with substrate concentration at different inhibitor concentration is well in accordance with the theory of competitive inhibition.<sup>20</sup> The data fitted to the competitive inhibition model resulted in a  $K_i$  value of  $85.0 \pm 5.0 \mu\text{mol}$  (calculated  $v_{\text{max}}$  remaining the same at  $160 \pm 10 \mu\text{mol/mnt/mg}$ ; Figure 5). The inhibition constant  $K_i$  obtained from inhibition of CRYP-2 by pNCS released from mesoporous media is in close proximity to values obtained for protein tyrosine phosphatase inhibited via other methods. This strongly supports our view of employment of inorganic nanostructured media for inhibition of enzymatic activity.

#### 4. Conclusions

Mesoporous materials (Al<sub>2</sub>O<sub>3</sub> and MCM-48) have been already shown to be promising hosts for delivery of small therapeutic drug molecules as mentioned earlier. The present study demonstrates viability of mesoporous materials to deliver a potent inhibitor of protein tyrosine phosphatase. As CRYP-2 enzyme is shown to be involved in hepatic carcinoma, its inhibition is of therapeutic importance. As already highlighted, the surface chemical functionality of the inorganic host materials plays an important role in the delivery of the payload. Oxide materials with different surface functionalities were successfully synthesized, characterized, and employed to form composites with inhibitor pNCS. As these materials release inhibitor in different amounts at different time scales, they are expected to exhibit different percentages of enzyme inhibition at different times. The slower inhibition rates of enzymatic activity exhibited by the mesoporous media compared to nonporous media need additional optimization. Optimization of the mesoporous media for producing various release rates (fast as well as slow) can be flexibly adopted by tuning pore morphology, structure, and surface chemistry. Additionally, the same oxide surface can be functionalized with more than one functional group (such as in "Janus" particles<sup>24</sup>) for uptake of various inhibitors and inhibition of different proteins. Optimization of the surface parameters of the delivery systems and amounts of pNCS to be withdrawn at different time intervals are ongoing, and once ascertained then pNCS would be allowed to interact with CRYP-2 in solution to determine the inhibition of the protein.

**Acknowledgment.** The authors thank I. S. Jarali (SSCU, IISc. Bangalore) for TGA and FTIR measurements and Amit Mondal (INI, IISc. Bangalore) for TEM.

**Supporting Information Available:** Nitrogen adsorption/desorption isotherms for various alumina and silica matrices

and pore size distribution obtained using BJH formulation (ref: Barrett, E. P.; Joyner, L. G.; Halenda, P. P. *J. Am. Chem. Soc.* **1951**, 73, 373) for bare Al<sub>2</sub>O<sub>3</sub> and MCM-48 (supporting Figure 1). Comparison of pH and activity profiles of the pTP domain (supporting Table 1). This material is available free of charge via the Internet at <http://pubs.acs.org>.

#### References and Notes

- (1) Barisoni, L.; Kriz, W.; Mundel, P.; D'Agati, V. *J. Am. Chem. Nephrol.* **1999**, 10, 51–61.
- (2) Wiggins, R. C.; Wiggins, J. E.; Goyal, M.; Wharram, B. L.; Thomas, P. E. *Genomics* **1995**, 27, 174–181.
- (3) Seimiya, H.; Tsuruo, T. *J. Biol. Chem.* **1998**, 273, 21187–21193.
- (4) Aguiar, R. C.; Yakushijin, Y.; Kharbanda, S.; Tiwari, S.; Freeman, G. J.; Shipp, M. A. *Blood* **1999**, 94, 2403–2413.
- (5) Motiwala, T.; Kutay, H.; Ghoshal, K.; Bai, S.; Seimiya, H.; Tsuruo, T.; Suster, S.; Morrison, C.; Jacob, S. T. *Proc. Natl. Acad. Sci.* **2004**, 101, 13844–13849.
- (6) Wiesmann, C.; Barr, K. J.; Kung, J.; Zhu, J.; Erlanson, D. A.; Shen, W.; Fahr, B. J.; Zhong, M.; Taylor, L.; Randal, M.; McDowell, R. S.; Hansen, S. K. *Nat. Struct. Mol. Biol.* **2004**, 11, 730–736.
- (7) Anderson, J. N.; Mortensen, O. H.; Peters, G. H.; Drake, P. G.; Iversen, L. F.; Olsen, O. H.; Jansen, P. G.; Andersen, H. S.; Tonks, N. K.; Moller, N. P. H. *Mol. Cell Biol.* **2001**, 21, 7117–7136.
- (8) Elchebly, M.; Payette, P.; Michaliszyn, E.; Cromlish, W.; Collins, S.; Loy, A. L.; Normandin, D.; Cheng, A.; Himms-Hagen, J.; Chang, C. C.; Ramachandran, C.; Resser, M. J.; Tremblay, M. L. *Science* **1999**, 283, 1544–1548.
- (9) Puius, Y. A.; Zhao, Y.; Sullivan, M.; Lawrence, D. S.; Almo, S. C.; Zhang, Z.-Y. *Proc. Natl. Acad. Sci.* **1997**, 94, 13420–13425.
- (10) Vallet-Regi, M.; Rámila, A.; del Real, R. P.; Perez-Pariente, J. *Chem. Mater.* **2001**, 13, 308–311.
- (11) Vinu, A.; Miyahara, M.; Ariga, K. *J. Nanosci. Nanotech.* **2006**, 6, 1510–1532.
- (12) Slowing, I. I.; Trewyn, B. G.; Lin, V. S.-Y. *J. Am. Chem. Soc.* **2007**, 129, 8845–8849.
- (13) Das, S. K.; Kapoor, S.; Yamada, H.; Bhattacharyya, A. J. *Mesopor. Micropor. Mater.* **2009**, 118, 267–272.
- (14) Kapoor, S.; Hegde, R.; Bhattacharyya, A. J. *J. Controlled Release* **2009**, 140, 34–39.
- (15) Radin, S.; Chen, T.; Ducheyne, P. *Biomaterials* **2009**, 30, 850–858.
- (16) Guo, S.; Li, D.; Zhang, L.; Li, J.; Wang, E. *Biomaterials* **2009**, 30, 1881–1889.
- (17) Hudson, S. P.; Padera, R. F.; Langer, R.; Kohane, D. S. *Biomaterials* **2008**, 29, 4045–4055.
- (18) Girish, T. S.; Gopal, B. *Protein: Struct., Funct., Bioinf.* **2007**, 68, 1011–1015.
- (19) Girish, T. S.; Gopal, B. *Acta Crystallogr.* **2005**, F61, 381–383.
- (20) Equations for Michaelis–Menten:  $v = (v_{\text{max}}[S]) / ([S] + K_m)$  and competitive inhibition  $v = (v_{\text{max}}[S]) / ([S] + K_m(1 + ([I]/K_i)))$ , where  $[S]$  = substrate concentration,  $v_{\text{max}}$  = maximum velocity for reaction,  $K_m$  = Michaelis–Menten constant,  $K_i$  = inhibition dissociation constant, and  $[I]$  = inhibitor concentration.
- (21) Socrates, G. *Infrared characteristic group frequencies*; John Wiley: New York, 1980.
- (22) Hair, M. L. *Infrared spectroscopy in surface chemistry*; Marcel Dekker: New York, 1967.
- (23) Rámila, A.; Muñoz, B.; Pérez-Pariente, J.; Vallet-Regi, M. *J. Sol-Gel Sci. Technol.* **2003**, 26, 1199–1202.
- (24) Perro, A.; Reculosa, A.; Ravaine, S.; Bourgeat-Lami, E.; Duguët, E. *J. Mater. Chem.* **2005**, 15, 3745–3760.

JP910166H